optica

Pathway-resolved photoelectron emission in dissociative ionization of molecules

X. Gong,[1] P. He,[2] Q. Song,[1] Q. Ji,[1] K. Lin,[1] W. Zhang,[1] P. Lu,[1] H. Pan,[1] J. Ding,[1] H. Zeng,[1,3,5] F. He,[2,6] and J. Wu[1,4,7]

[1]State Key Laboratory of Precision Spectroscopy, East China Normal University, Shanghai 200062, China
[2]Key Laboratory of Laser Plasmas (Ministry of Education) and Department of Physics and Astronomy, Collaborative Innovation Center for IFSA (CICIFSA), Shanghai Jiao Tong University, Shanghai 200240, China
[3]Synergetic Innovation Center of Quantum Information and Quantum Physics, University of Science and Technology of China, Anhui 230026, China
[4]Collaborative Innovation Center of Extreme Optics, Shanxi University, Taiyuan, Shanxi 030006, China
[5]e-mail: hpzeng@phy.ecnu.edu.cn
[6]e-mail: fhe@sjtu.edu.cn
[7]e-mail: jwu@phy.ecnu.edu.cn

Received 4 April 2016; revised 18 May 2016; accepted 25 May 2016 (Doc. ID 262391); published 10 June 2016

Electron–ion coincidence detection allows one to visualize the ultrafast chemical reactions of molecules in strong laser fields. Here, by measuring the photoelectron angular distribution (PAD) of H_2 in strong laser fields correlated to different pathways, i.e., direct ionization when the internuclear distance is small, or ionization after the molecular bond stretches to a large internuclear distance, we uncover the roles of the molecular orientation and internuclear distance in the dissociative ionization of H_2. As compared to the first dissociation pathway, the regular nodal structures on the concentric above-threshold ionization circles vanish for the second pathway, which are numerically validated by the quantum simulations. Pathway-resolved PADs assisted by electron–ion coincidence detection open new possibilities to probe the rich dynamics of molecules in strong laser fields, in particular to image the instantaneous geometry of molecules.

OCIS codes: (020.2649) Strong field laser physics; (020.4180) Multiphoton processes; (260.7120) Ultrafast phenomena.

http://dx.doi.org/10.1364/OPTICA.3.000643

Single- and multiphoton-ionization of atoms and molecules in external fields have been well studied to probe the electronic and nuclear dynamics [1–3]. The photoelectron angular distribution (PAD) [4] of the above threshold ionization (ATI) in the multiphoton ionization regime manifests itself as multiple concentric circles shaped with regular nodal structures [5–8]. In tunneling ionization, the released electron wave packet flows mainly along the laser polarization axis without the regular nodal structure [9]. The tunneled electron mostly ends at zero momentum along the field direction of the linearly polarized pulse [10], or is angularly streaked by an elliptically polarized pulse [11].

As compared to atoms, the PADs of molecules depend not only on the binding energies but also on the molecular orientation and geometry [12–14] at the instant of electron release. It imprints the instantaneous electronic and nuclear structures of the molecule [15,16], which makes it very attractive for real-time imaging of the structure of an isolated molecule [17] and to probe the rich dynamics of photoionization [4,18,19]. A molecule in strong laser fields may undergo different chemical reaction pathways. One problem would be how the molecular orientation and internuclear distance play roles for these different pathways. Conversely and more challengingly, is it possible to experimentally disentangle the coexisting different dynamics for various reaction pathways? Pathway-resolved PADs assisted by electron–ion coincidence detection open the possibility to uncover the concurrent molecular-orientation and internuclear-distance dependences.

In this Letter, by resolving the multiphoton ATI of H_2 into various dissociation pathways, we observe distinct PADs driven by an intense femtosecond laser pulse. We identified two dissociative ionization pathways, as shown in Fig. 1(a). First, H_2 is singly ionized around its equilibrium distance, and the resultant H_2^+ undergoes bond-softening dissociation [20,21] by absorbing one extra photon. Second, the neutral H_2 may be excited to an intermediate state by absorbing multiple photons and stretch to a large internuclear distance. The stretched H_2 may absorb few extra photons, giving birth to a free electron, meanwhile launching the nuclear wave packet on the dissociative state, which ultimately gains a little kinetic energy. We name these two dissociation pathways, respectively, post-ionization dissociation [22–24] and stretched-bond ionization pathways. Here we observe distinct PADs correlated to the post-ionization dissociation and stretched-bond ionization pathways. This is inherent and unique for molecules as compared to atoms, which cannot be revealed by tracing the PAD correlated to the non-dissociative H_2^+ [25].

Our experimental measurements are performed in an ultrahigh vacuum chamber of cold target recoil ion momentum spectroscopy (COLTRIMS) [26,27]. Femtosecond laser pulses with various wavelengths and temporal durations are focused onto a supersonic

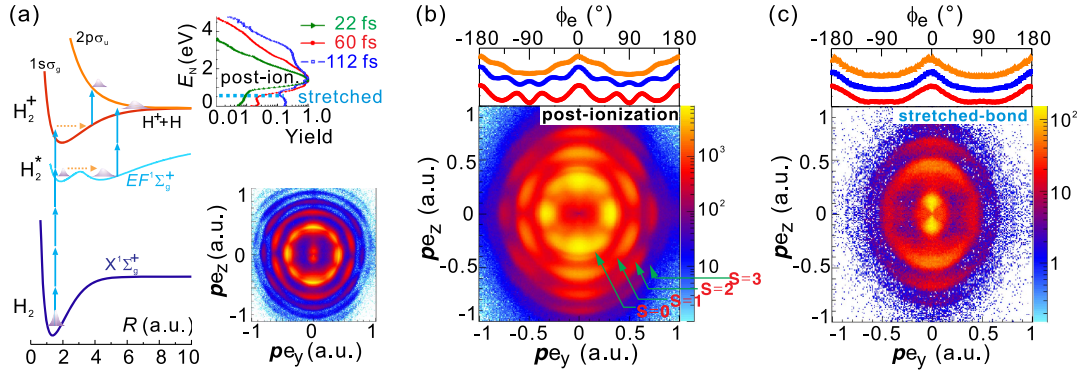

Fig. 1. (a) Schematic diagram of the post-ionization dissociation and stretched-bond ionization pathways in multiphoton ionization of H_2. The insets show the normalized kinetic energy release distribution of the $H^+ + H$ (top, driven by laser pulses of different temporal durations), and the PAD correlated to H_2^+ (bottom) measured for the 60 fs, 395 nm UV pulse at $I_0 = 1.1 \times 10^{14}$ W/cm^2. (b), (c) Measured PADs correlated to (b) the post-ionization dissociation and (c) the stretched-bond ionization pathways of the $H_2(1, 0)$ channel. The top panels of (b) and (c) are the electron kinetic energy-integrated PADs of three ATI orders, where ϕ_e is defined with respect to the laser polarization vector along the z axis.

gas jet of H_2 by a concave silver mirror ($f = 7.5$ cm) inside the vacuum chamber. The three-dimensional momentum vectors of the measured protons and electrons are reconstructed from the times of flight and positions detected by two time- and position-sensitive microchannel plate detectors at opposite ends of the spectrometer (Supplement 1). In the following, we will first use a 60 fs, 395 nm ultraviolet (UV) pulse to demonstrate the pathway-resolved PADs of the $H_2 + m\hbar\omega \rightarrow H^+ + H + e$ channel with m being an integer, labeled $H_2(1, 0)$, and then its dependences on the field intensity and central wavelength of the laser pulses. Here, we use the concept of pathway to label the dissociation process as widely used in the dissociative ionization of H_2 by laser fields of modest intensities [23,24]. As compared to previous works using weak fields of high photon energies [28,29], a yield ratio of 3:1 between the dissociative and non-dissociative single ionization pathways is observed in our experiments.

The two dissociation pathways give distinct nuclear kinetic energy release E_N. For the post-ionization dissociation, the E_N peaks around 1.5 eV, which is consistent with previous measurements [22–24]. On the other hand, stretched-bond ionization happens when the internuclear distance is already very large, resulting in a low E_N, as shown in the inset (top) in Fig. 1(a). Besides the E_N, the emitted electrons associated with these two pathways present distinct PADs. The post-ionization electron spectra are collected in coincidence with the H^+ fragment energy of 1.5 ± 0.5 eV. The stretched-bond electron spectra are collected in coincidence with the H^+ fragment energy of 0.25 ± 0.25 eV. Using this coincidence, we separate these two different pathways and show the corresponding photoelectron spectra in Figs. 1(b) and 1(c). The regular nodal structures observed on the concentric ATI circles of the post-ionization dissociation pathway [Fig. 1(b)] disappear for the stretched-bond ionization pathway [Fig. 1(c)]. The electron kinetic-energy-integrated PADs of three low ATI orders are correspondingly displayed in the top insets of Figs. 1(b) and 1(c). As compared to previous work on the electron detachment processes of a molecular anion [14], here we directly resolve the PADs into various dissociative ionization pathways of a neutral molecule. As shown in Fig. 2, distinct PADs of two dissociative ionization pathways are observed for a wide range of field intensity of the UV pulse from 0.5 to 1.5×10^{14} W/cm^2. To show that the pathway-resolved distinct PADs are not unique for the 395 nm UV pulse, we adjusted the central wavelength of the laser pulse using traveling-wave optical parametric amplifier superfluorescence. Similar to the 395 nm UV pulse, the post-ionization dissociation and stretched-bond ionization pathways are featured with distinct PADs when the wavelength is shorter than 550 nm. For instance, Figs. 2(g) and 2(h) display the pathway-resolved distinct PADs for a 510 nm femtosecond laser pulse.

Concentric ATI circles with regular nodal structures are typically observed for the multiphoton single ionization of atoms and molecules [5,7,30–32]. The regular nodal structure is understood as the intracycle interference of the released electronic wave packets [7,8,18,19], which also encodes the quantum number of the angular momentum of the freed electron [25,33,34]. As shown in Figs. 2(a), 2(c), and 2(e), the additional nodes on the near-threshold ionization ATI circle ($S = 0$) appear only at high field intensities and shift to lower energies due to the long-range Coulomb potential [33–36]. As displayed in the inset of Fig. 1(a), similar concentric ATI circles with regular nodal structures are observed for the non-dissociative H_2^+, which is mostly generated by ionizing H_2 around the equilibrium internuclear distance $R = 1.4$ a.u. Correspondingly, as shown in Fig. 3(a), the positions of the nodes and local maxima in the

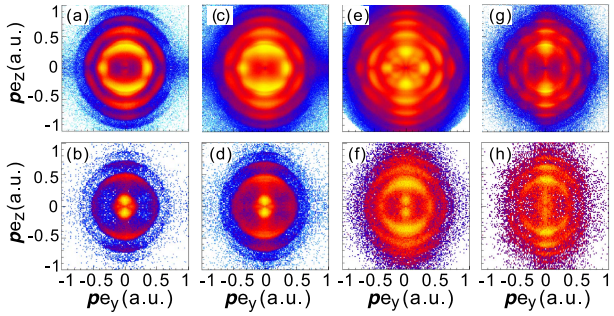

Fig. 2. Measured PADs correlated to the post-ionization dissociation (top row) and stretched-bond ionization (bottom row) pathways of the $H_2(1, 0)$ channel at various laser intensities and wavelengths. The laser intensities of the 60 fs, 395 nm UV pulse are set to be (a), (b) 0.5; (c), (d) 0.7; and (e), (f) 1.5×10^{14} W/cm^2. The central wavelength of the laser pulse is 510 nm in (g) and (h), and its intensity and temporal duration are 0.8×10^{14} W/cm^2 and 30 fs.

PAD of the post-ionization dissociation pathway are independent of the orientation of H_2.

The role of the molecular orientation in photoionization processes becomes significant when the electron is released at a large internuclear distance. As shown in Fig. 3(b), the PAD of the stretched-bond ionization pathway clearly depends on the orientation of H_2, especially for electrons emitting away from the field polarization direction, whose local maximal positions gradually change as marked by the white dashed curves. As shown in Fig. 3(c), the angular nodal structures sensitively depend on the molecular orientation. These fine structures are averaged out by integrating over the absolute value of the molecular orientation angle θ_{H+} from 0° to 180°, resulting in a tunneling-like PAD featured with dominant distribution along the polarization direction of the laser field. As illustrated in Fig. 1(a), one possible process for the stretched-bond ionization pathway is: first, H_2 absorbs four photons and is excited to an intermediate state, e.g., the double-well $EF^1\Sigma_g^+$ state about 13 eV above the ground state of H_2 [25,28,29,37,38]; second, the excited H_2 may stretch to a large internuclear distance around $R \sim 6$ a.u.; third, the stretched H_2 is singly ionized by absorbing two extra photons while the nuclear wave packet is tossed onto the dissociative potential surface and finally dissociates into $H + H^+$ with little E_N. The $EF^1\Sigma_g^+$ state is the most likely intermediate for the stretched-bond ionization pathway in our UV pulse because it lies in the proper energy range of four photons with the right parity for the dipole-allowed transition from the ground state $X^1\Sigma_g^+$ of H_2. Meanwhile, its double-well structure with the F-well around $R = 6$ a.u. increases the probability of observing the stretched-bond ionization pathway by freeing an electron at a large internuclear distance. As shown in the inset of Fig. 1(a), the stretched-bond ionization pathway is favored for laser pulses of long temporal durations in which the molecule has enough time to elongate to a large internuclear distance where the electron is freed. Here, a 22-fs UV pulse was generated by frequency doubling a precompressed few-cycle pulse from the output of a Ne-filled hollow fiber. The UV pulse was alternatively temporally stretched to 112 fs by inserting several pieces of fused silica glasses (Supplement 1).

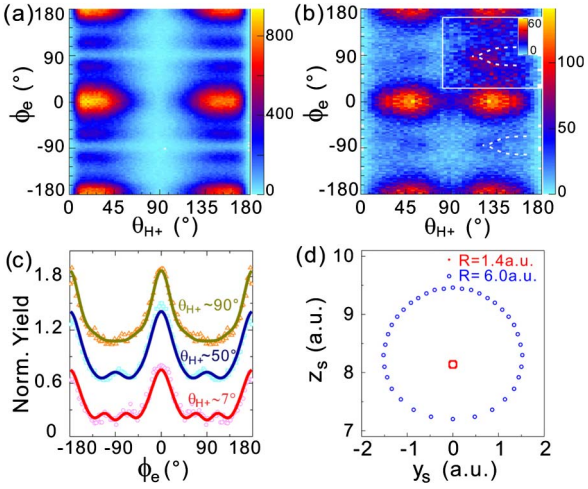

Fig. 3. (a), (b) PADs of the second-order ATI ($S = 1$) as a function of the molecular orientation correlated to the (a) post-ionization dissociation and (b) stretched-bond ionization pathways. To increase the visibility, the inset of (b) (top right) zooms in the molecular-orientation-dependent PADs with a different color bar from 0 to 60 counts where the positions of the local maxima are marked by the white dashed lines. (c) The normalized and vertically offset slices of the PAD at $\theta_{H+} = 7°$, 50°, and 90° extracted from (b), which are fitted by using Legendre polynomials of $\sum_{n=0}^{5} C_{2n} P_{2n}(\cos(\phi_e))$ with proper coefficients C_{2n}. (d) Calculated saddle positions in the y–z plane for internuclear distance $R = 1.4$ and 6.0 a.u.

We numerically simulated the time-dependent Schrödinger equation (TDSE) with the single active electron approximation to test the PADs (Supplement 1). We calculated the single-ionization-induced PADs at $R = 1.4$ and 6 a.u., standing for the electron release at small and large internuclear distances, respectively. The simulated PADs for $R = 6$ a.u. are shown in Figs. 4(a)–4(c), respectively corresponding to the absolute value of the cross angles $|\theta_{H+}| = 0°$, 30°, and 60°. Hence, for example, Fig. 4(b) is the averaged results for $\theta_{H+} = +30°$ and $-30°$, which preserves the left–right symmetry for the PAD. The fine structures of the simulated PADs vary as the molecule orients at different angles. As a result, the orientation-averaged overall PAD [Fig. 4(d)] is maximized along the polarization direction of the laser field. However, for $R = 1.4$ a.u., as shown in Figs. 4(e)–4(g), the simulated PADs are nearly independent of the molecular orientation. The regular nodal structures on the ATI circles thus survive in the overall PAD after the orientation average. Figures 4(d) and 4(h) capture the main features of the experiments and thus confirm the roles of molecular orientation at various internuclear distances for two different dissociative ionization pathways. One may note that our modeled TDSE cannot precisely describe the electronic state of $EF^1\Sigma_g^+$ at $R = 6$ a.u.; however, our test simulations show that the PADs are not sensitive to the details of the initial electronic state of the bond-stretched molecule, but are dominated by the orientation of the molecular axis with respect to the laser polarization.

To understand the orientation-dependent PADs for electron release at various internuclear distances, Fig. 3(d) shows the calculated saddle position (y_s, z_s) in the plane composing the molecular axis and the laser electric field by setting $\partial V(R, x, y, z)/\partial y = 0$, $\partial[V(R, x, y, z) + zE]/\partial z = 0$ and scanning the molecular orientation angle from 0 to 2π. The instantaneous electric field was $E = -0.053$ a.u. and pointed to $-z$. The corresponding Keldysh parameters are 1.4 and 2.3 for the modeled molecule with internuclear distances of $R = 1.4$ and 6 a.u., respectively, in which range the tunneling picture of the electron release still works well, as demonstrated in Refs. [39,40]. When the internuclear distance is $R = 1.4$ a.u., (y_s, z_s) nearly does not change when the molecular orientation changes. However,

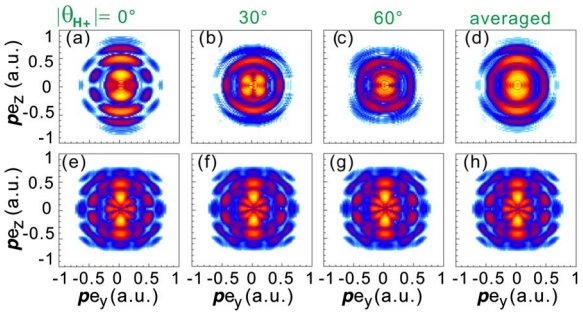

Fig. 4. Simulated PADs of the single ionization of H_2 at (a)–(d) $R = 6.0$ a.u., and (e)–(h) $R = 1.4$ a.u. The laser intensities for the top and bottom rows are 4.0×10^{13} and 1.5×10^{14} W/cm^2, respectively.

(y_s, z_s) scatters in a relative large area when the internuclear distance is $R = 6$ a.u. This will introduce different initial phases and subsequent Coulomb actions of the nuclei on the outgoing electrons. Hence, for different molecular orientations, the structure of the PADs, for example, the nodal structure ruled by the interference of the released electrons, are clearly different, which qualitatively explains the experimental observations and theoretical calculations.

In summary, by resolving the multiphoton single ionization of H_2 into various channels, we have observed distinct PADs for the post-ionization dissociation and stretched-bond ionization pathways. As compared to the post-ionization dissociation pathway, the regular nodes on the concentric ATI circles vanish for the stretched-bond ionization pathway. This is attributed to the molecular-orientation- and internuclear-distance-dependent photoelectron emission. By measuring the ejected electrons and ions in coincidence, the pathway-resolved PADs provide a powerful tool for revealing the complex dynamics of molecules in strong laser fields.

Funding.
"Eastern Scholar" Program of Shanghai; National Natural Science Foundation of China (NSFC) (11425416, 11374103, 11121504, 11322438, 11574205, 11434005).

Acknowledgment. We thank R. Dörner, Y. Liu, and M. Li for fruitful discussions.

See Supplement 1 for supporting content.

REFERENCES

1. D. Akoury, K. Kreidi, T. Jahnke, Th. Weber, A. Staudte, M. Schöffler, N. Neumann, J. Titze, L. Ph. H. Schmidt, A. Czasch, O. Jagutzki, R. A. Costa Fraga, R. E. Grisenti, R. Díez Muiño, N. A. Cherepkov, S. K. Semenov, P. Ranitovic, C. L. Cocke, T. Osipov, H. Adaniya, J. C. Thompson, M. H. Prior, A. Belkacem, A. L. Landers, H. Schmidt-Böcking, and R. Dörner, Science **318**, 949 (2007).
2. C. E. Liekhus-Schmaltz, I. Tenney, T. Osipov, A. Sanchez-Gonzalez, N. Berrah, R. Boll, C. Bomme, C. Bostedt, J. D. Bozek, S. Carron, R. Coffee, J. Devin, B. Erk, K. R. Ferguson, R. W. Field, L. Foucar, L. J. Frasinski, J. M. Glownia, M. Gühr, A. Kamalov, J. Krzywinski, H. Li, J. P. Marangos, T. J. Martinez, B. K. McFarland, S. Miyabe, B. Murphy, A. Natan, D. Rolles, A. Rudenko, M. Siano, E. R. Simpson, L. Spector, M. Swiggers, D. Walke, S. Wang, Th. Weber, P. H. Bucksbaum, and V. S. Petrovic, Nat. Commun. **6**, 8199 (2015).
3. P. Agostini, F. Fabre, G. Mainfray, and G. Petite, Phys. Rev. Lett. **42**, 1127 (1979).
4. K. L. Reid, Annu. Rev. Phys. Chem. **54**, 397 (2003).
5. D. G. Arbó, K. L. Ishikawa, K. Schiessl, E. Persson, and J. Burgdörfer, Phys. Rev. A **81**, 021403(R) (2010).
6. Y. Huismans, A. Rouzée, A. Gijsbertsen, J. H. Jungmann, A. S. Smolkowska, P. S. W. M. Logman, F. Lépine, C. Cauchy, S. Zamith, T. Marchenko, J. M. Bakker, G. Berden, B. Redlich, A. F. G. van der Meer, H. G. Muller, W. Vermin, K. J. Schafer, M. Spanner, M. Yu. Ivanov, O. Smirnova, D. Bauer, S. V. Popruzhenko, and M. J. J. Vrakking, Science **331**, 61 (2011).
7. T. Yan and D. Bauer, Phys. Rev. A **86**, 053403 (2012).
8. M. Li, J. W. Geng, H. Liu, Y. Deng, C. Wu, L. Y. Peng, Q. Gong, and Y. Liu, Phys. Rev. Lett. **112**, 113002 (2014).
9. A. Ludwig, J. Maurer, B. W. Mayer, C. R. Phillips, L. Gallmann, and U. Keller, Phys. Rev. Lett. **113**, 243001 (2014).
10. Y. Huismans, A. Gijsbertsen, A. S. Smolkowska, J. H. Jungmann, A. Rouzée, P. S. W. M. Logman, F. Lépine, C. Cauchy, S. Zamith, T. Marchenko, J. M. Bakker, G. Berden, B. Redlich, A. F. G. van der Meer, M. Yu. Ivanov, T.-M. Yan, D. Bauer, O. Smirnova, and M. J. J. Vrakking, Phys. Rev. Lett. **109**, 013002 (2012).
11. L. Holmegaard, J. L. Hansen, L. Kalhøj, S. L. Kragh, H. Stapelfeldt, F. Filsinger, J. Küpper, G. Meijer, D. Dimitrovski, M. Abu-samha, C. P. J. Martiny, and L. B. Madsen, Nat. Phys. **6**, 428 (2010).
12. V. Kumarappan, L. Holmegaard, C. Martiny, C. B. Madsen, T. K. Kjeldsen, S. S. Viftrup, L. B. Madsen, and H. Stapelfeldt, Phys. Rev. Lett. **100**, 093006 (2008).
13. Z. Hu, X. Lai, X. Liu, and J. Chen, Phys. Rev. A **89**, 043401 (2014).
14. H. Hultgren and I. Yu. Kiyan, Phys. Rev. A **84**, 015401 (2011).
15. M. Meckel, D. Comtois, D. Zeidler, A. Staudte, D. Pavičić, H. C. Bandulet, H. Pépin, J. C. Kieffer, R. Dörner, D. M. Villeneuve, and P. B. Corkum, Science **320**, 1478 (2008).
16. Q. Ji, S. Cui, X. You, X. Gong, Q. Song, K. Lin, H. Pan, J. Ding, H. Zeng, F. He, and J. Wu, Phys. Rev. A **92**, 043401 (2015).
17. J. B. Williams, C. S. Trevisan, M. S. Schöffler, T. Jahnke, I. Bocharova, H. Kim, B. Ulrich, R. Wallauer, F. Sturm, T. N. Rescigno, A. Belkacem, R. Dörner, Th. Weber, C. W. McCurdy, and A. L. Landers, Phys. Rev. Lett. **108**, 233002 (2012).
18. R. Gopal, K. Simeonidis, R. Moshammer, Th. Ergler, M. Dürr, M. Kurka, K.-U. Kühnel, S. Tschuch, C.-D. Schröter, D. Bauer, J. Ullrich, A. Rudenko, O. Herrwerth, Th. Uphues, M. Schultze, E. Goulielmakis, M. Uiberacker, M. Lezius, and M. F. Kling, Phys. Rev. Lett. **103**, 053001 (2009).
19. X. Xie, S. Roither, D. Kartashov, E. Persson, D. G. Arbó, L. Zhang, S. Gräfe, M. S. Schöffler, J. Burgdörfer, A. Baltuška, and M. Kitzler, Phys. Rev. Lett. **108**, 193004 (2012).
20. A. D. Bandrauk and M. L. Sink, J. Chem. Phys. **74**, 1110 (1981).
21. P. H. Bucksbaum, A. Zavriyev, H. G. Muller, and D. W. Schumacher, Phys. Rev. Lett. **64**, 1883 (1990).
22. J. Wu, M. Kunitski, M. Pitzer, F. Trinter, L. Ph. H. Schmidt, T. Jahnke, M. Magrakvelidze, C. B. Madsen, L. B. Madsen, U. Thumm, and R. Dörner, Phys. Rev. Lett. **111**, 023002 (2013).
23. D. Ray, F. He, S. De, W. Cao, H. Mashiko, P. Ranitovic, K. P. Singh, I. Znakovskaya, U. Thumm, G. G. Paulus, M. F. Kling, I. V. Litvinyuk, and C. L. Cocke, Phys. Rev. Lett. **103**, 223201 (2009).
24. X. Gong, P. He, Q. Song, Q. Ji, H. Pan, J. Ding, F. He, H. Zeng, and J. Wu, Phys. Rev. Lett. **113**, 203001 (2014).
25. T. Wilbois and H. Helm, Phys. Rev. A **84**, 053407 (2011).
26. J. Ullrich, R. Moshammer, A. Dorn, R. Dörner, L. Ph. H. Schmidt, and H. Schmidt-Böcking, Rep. Prog. Phys. **66**, 1463 (2003).
27. O. Jagutzki, A. Cerezo, A. Czasch, R. Dörner, M. Hattaß, M. Huang, V. Mergel, U. Spillmann, K. U. Pfleger, Th. Weber, H. S. Böcking, and G. D. W. Smith, IEEE Trans. Nucl. Sci. **49**, 2477 (2002).
28. C. Cornaggia, A. Giusti-Suzor, and Ch. Jungen, J. Chem. Phys. **87**, 3934 (1987).
29. E. F. McCormack, S. T. Pratt, J. L. Dehmer, and P. M. Dehmer, J. Chem. Phys. **92**, 4734 (1990).
30. R. Wiehle, B. Witzel, H. Helm, and E. Cormier, Phys. Rev. A **67**, 063405 (2003).
31. P. Kaminski, R. Wiehle, V. Renard, A. Kazmierczak, B. Lavorel, O. Faucher, and B. Witze, Phys. Rev. A **70**, 053413 (2004).
32. Ph. A. Korneev, S. V. Popruzhenko, S. P. Goreslavski, T.-M. Yan, D. Bauer, W. Becker, M. Kübel, M. F. Kling, C. Rödel, M. Wünsche, and G. G. Paulus, Phys. Rev. Lett. **108**, 223601 (2012).
33. Z. Chen, T. Morishita, A.-T. Le, M. Wickenhauser, X. M. Tong, and C. D. Lin, Phys. Rev. A **74**, 053405 (2006).
34. T. Marchenko, H. G. Muller, K. J. Schafer, and M. J. J. Vrakking, J. Phys. B **43**, 095601 (2010).
35. D. G. Arbó, S. Yoshida, E. Persson, K. I. Dimitriou, and J. Burgdörfer, Phys. Rev. Lett. **96**, 143003 (2006).
36. T. Morishita and C. D. Lin, Phys. Rev. A **87**, 063405 (2013).
37. J. Fernández and F. Martín, Phys. Rev. A **75**, 042712 (2007).
38. P. Ranitovic, C. W. Hogle, P. Rivière, A. Palacios, X. Tong, N. Toshima, A. González-Castrillo, L. Martin, F. Martín, M. M. Murnane, and H. Kapteyn, Proc. Natl. Acad. Sci. USA **111**, 912 (2014).
39. R. Boge, C. Cirelli, A. S. Landsman, S. Heuser, A. Ludwig, J. Maurer, M. Weger, L. Gallmann, and U. Keller, Phys. Rev. Lett. **111**, 103003 (2013).
40. M. Klaiber, K. Z. Hatsagortsyan, and C. H. Keitel, Phys. Rev. Lett. **114**, 083001 (2015).